

# Droplet-supported liquid-liquid lateral phase separation as a step to floating protein heterostructures

Received: 5 October 2024

Accepted: 12 February 2025

Published online: 23 February 2025



Haixu Chen<sup>1,5</sup>, Zhengbin Han<sup>2</sup>, Shengliang Wang<sup>1</sup>, Mei Zhu<sup>1</sup>, Lei Wang<sup>1</sup>,  
Youping Lin<sup>1</sup>, Xiaoliang Wang<sup>1</sup>, Yide Zhang<sup>1</sup>, Wei Wang<sup>1,3</sup>, Mei Li<sup>4</sup>,  
Xiaoman Liu<sup>1</sup>, Stephen Mann<sup>4</sup>✉ & Xin Huang<sup>1</sup>✉

Liquid-liquid phase separation plays an important role in many natural and technological processes. Herein, we implement lateral microphase separation at the surface of oil micro-droplets suspended in water to prepare a range of discrete floating protein/polymer continuous two-dimensional (2D) heterostructures with variable interfacial domain structures and dynamics. We show that gel-like domains of bovine serum albumin (BSA) co-exist with fluid-like polyvinyl alcohol (PVA) regions at the oil droplet surface to produce floating heterostructures comprising a 2D phase-separated protein mesh or an array of discrete mobile protein rafts depending on the conditions employed. Enzymes are embedded in the discontinuous BSA domains to produce droplet-supported microphase-separated 2D reaction scaffolds that can be tuned for interfacial catalysis. Taken together, our work has general implications for the structural and functional augmentation of oil droplet interfaces and contributes to the surface engineering and functionality of droplet-based micro-reactors.

The control of phase separation in mixtures of immiscible solvents or aqueous solutions of incompatible solutes is an important consideration in areas of cosmetics<sup>1</sup>, food processing<sup>2</sup>, enhanced oil recovery<sup>3</sup>, micro-reactor technology<sup>4</sup>, bioengineering<sup>5</sup>, complex emulsion reconstruction<sup>6</sup>, and protocell modeling<sup>7–13</sup>. Aqueous liquid-liquid two-phase separation in mixtures of incompatible water-soluble macromolecules is associated with segregative (demixing) and associative (coacervation) processes<sup>14,15</sup>, and has been used for the enrichment of DNA<sup>16</sup>, extraction of proteins<sup>17</sup>, and construction of artificial cells capable of programmable spatial organization<sup>18</sup>, microreactor processing<sup>19</sup>, bacterial capture and killing<sup>20</sup>, and microscale motility<sup>21,22</sup>. Although three-dimensional

(3D) phase separation is diverse and has many important applications, two-dimensional (2D) phase separation is strongly influenced by spatial confinement, structural asymmetry and distinctive interfacial functions and dynamics such as entropy-driven pattern formation<sup>23</sup>, restricted interfacial molecular diffusion<sup>24</sup>, and controlled movement<sup>25</sup>. 2D phase separation also plays an important role in the functioning of living cells<sup>26</sup>. Specific membrane proteins are enriched in lipid rafts for aiding signal communication<sup>27</sup> and molecular internalization<sup>28</sup>, and internal microstructures such as the endoplasmic reticulum<sup>29</sup>, mitochondria<sup>30</sup> and lipid droplets<sup>24</sup> are associated with surface-segregated components that mediate intracellular interactions between organelles<sup>31</sup>.

<sup>1</sup>MIIT Key Laboratory of Critical Materials Technology for New Energy Conversion and Storage, School of Chemistry and Chemical Engineering, Harbin Institute of Technology, Harbin, China. <sup>2</sup>HIT Center for Life Sciences, School of Life Science and Technology, Harbin Institute of Technology, Harbin, China.

<sup>3</sup>State Key Laboratory of Urban Water Resource and Environments, Harbin Institute of Technology, Harbin, China. <sup>4</sup>Max Planck Bristol Centre for Minimal Biology, Centre for Protolife Research and Centre for Organized Matter Chemistry, School of Chemistry, University of Bristol, Bristol, UK. <sup>5</sup>Present address: State Key Laboratory of Urban Water Resource and Environments, Harbin Institute of Technology, Harbin, China. ✉e-mail: [s.mann@bristol.ac.uk](mailto:s.mann@bristol.ac.uk); [xinhuang@hit.edu.cn](mailto:xinhuang@hit.edu.cn)

Although various assembly strategies involving liposomes<sup>32</sup>, polymersomes<sup>33</sup>, oil-water emulsion microdroplet<sup>34,35</sup> or coacervate micro-droplets<sup>18,20,36–38</sup> have been reported as pathways to functional micro-compartments, the use of 2D phase separation for the modulation of interfacial structure and functionality in discrete enclosed micro-ensembles has not been explored in detail<sup>23,25,39–41</sup>. In this paper, we produce continuous floating heterostructures with interfacial morphology and functionality by spontaneous lateral microphase separation of an aqueous mixture of bovine serum albumin (BSA) and polyvinyl alcohol (PVA) at the surface of oil micro-droplets. A range of different phase-separated modes with variable interfacial domain structures and dynamics is demonstrated. In each case, gel-like BSA domains coexist with fluid-like PVA regions to produce floating droplet-based heterostructures comprising a continuous protein 2D mesh or an array of discrete protein rafts. The latter exhibit translational motion across the oil droplet surface depending on their domain size and area ratio and the viscosity of the aqueous medium. We demonstrate that active enzymes can be immobilized in the discontinuous BSA domains to produce discrete floating protein/PVA droplet heterostructures capable of spatially modulated interfacial catalysis. Our work has general implications for the structural and functional augmentation of oil droplet interfaces, provides a route to the spontaneous assembly of discrete continuous protein/polymer phase-separated heterostructures and

offers a step to the surface engineering of droplet-based micro-reactors for potential use in biocatalytic processing.

## Results

### Oil droplet-templated liquid-liquid lateral microphase separation

Gentle shaking of an aqueous mixture of BSA ( $M_w = 66.5$  kDa) and PVA ( $M_w = 18$  kDa) at pH 7 and room temperature with tributyrin produced a dispersion of stabilized oil-in-water droplets with a mean diameter of 42  $\mu\text{m}$ . 2D and 3D confocal laser scanning microscopy (CLSM) fluorescence images indicated that emulsification was associated with five different modes of spontaneous protein/polymer lateral microphase separation on the surface of the individual tributyrin microdroplets. The modes included binary phase-separated microstructures (PVA-in-BSA and BSA-in-PVA), along with more complex nested arrangements (BSA-in-PVA-in-BSA, PVA-in-BSA-in-PVA, hybrid PVA-in-BSA/PVA-in-BSA-in-PVA) (Fig. 1a–e and Supplementary Fig. 1). Changes in the concentrations of BSA and PVA produced different relative percentages of the various floating microstructures with PVA-in-BSA and BSA-in-PVA being the dominant 2D microphase organizations (Fig. 1f, and Supplementary Table 1). Irregularly shaped discontinuous PVA microdomains dispersed in a continuous BSA phase were observed when the protein and polymer concentrations were equal or greater than 5 mg/mL and equal or less than 0.5 mg/mL, respectively. The size of the floating PVA domains increased as the BSA and PVA

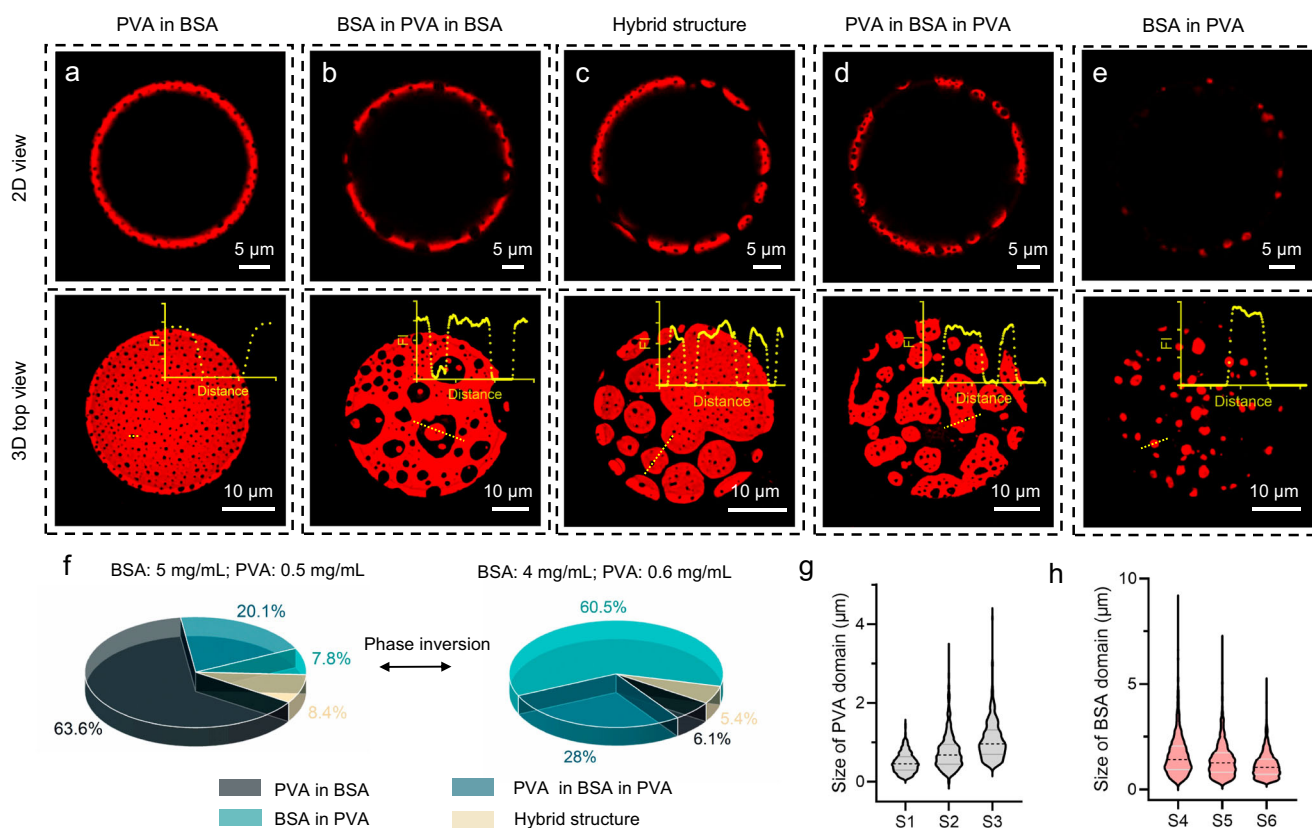


**Fig. 1 | Lateral microphase separation on oil-in-water droplet interfaces.** 2D (top row) and 3D top view (bottom row) CLSM fluorescence images of five modes of microphase separation observed on the surface of tributyrin oil droplets suspended in water at pH 7; PVA-in-BSA (a), BSA-in-PVA-in-BSA (b), hybrid of PVA-in-BSA and PVA-in-BSA-in-PVA (c), PVA-in-BSA-in-PVA (d) and BSA-in-PVA (e). BSA is labeled with rhodamine B isothiocyanate (RBITC; red fluorescence). Insets on bottom row: fluorescence intensity profiles recorded at selected positions on the droplet surfaces (yellow dashed lines in top views). f Distribution of different microphase separation modes at different BSA and PVA concentrations. Size of PVA

(g) and BSA (h) discontinuous domains for different concentrations; samples: S1, BSA 9 mg/mL, PVA 0.1 mg/mL; S2, BSA 8 mg/mL, PVA 0.2 mg/mL; S3, BSA 7 mg/mL, PVA 0.3 mg/mL; S4, BSA 3 mg/mL, PVA 0.7 mg/mL; S5, BSA 2 mg/mL, PVA 0.8 mg/mL; S6, BSA 1 mg/mL, PVA 0.9 mg/mL. Data in (g, h) are presented as violin plots, black dashed lines indicate median and gray solid line indicate quartiles ( $n = 1000$  domains examined over 3 independent experiments). All relevant experiments in (a–e) are performed independently at least three times with similar results. Source data are provided as a Source Data file.

concentrations were progressively decreased and increased, respectively. For example, changing the BSA and PVA concentrations from 9 to 7 mg/mL and from 0.1 to 0.3 mg/mL, respectively, extended the PVA domains from *ca.* 0.5 to 1.1  $\mu\text{m}$  in dimension (Fig. 1g). Consequently, decreasing the protein concentration below 5 mg/mL (PVA > 0.5 mg/mL) resulted in phase inversion with the relative proportions of 2D PVA-in-BSA and BSA-in-PVA microstructures changing from approximately 64 and 8% (BSA: PVA = 5 mg/mL: 0.5 mg/mL) to 6 and 61% (BSA: PVA = 4 mg/mL: 0.6 mg/mL), respectively. The size of the irregularly shaped BSA domains was *ca.* 1.7  $\mu\text{m}$  at a BSA: PVA concentration ratio of 3 mg/mL: 0.7 mg/mL, and decreased to 1.2  $\mu\text{m}$  at a BSA: PVA concentration ratio of 1 mg/mL: 0.9 mg/mL (Fig. 1h).

Molecular dynamics (MD) simulations of BSA and PVA molecules placed near to an oil/water interface (Supplementary movie S1 and Supplementary Figs. 2 and 3) gave BSA-BSA and PVA-PVA intermolecular interaction energies of  $-2.8 \times 10^5$  and  $-7.6 \times 10^4$  kJ/mol, respectively (Supplementary Fig. 4). In contrast, the intermolecular interaction energy between BSA and PVA was  $-4.1 \times 10^3$  kJ/mol (Supplementary Fig. 4). The large free energy differences were consistent with microphase separation at the surface of the tributyrin oil droplets. We attributed the lower intermolecular interaction energy between PVA molecules to the prevalence of intramolecular rather than intermolecular hydrogen bonds at the oil-water interface (Supplementary Figs. 5 and 6). In comparison, multiple types of intermolecular

interactions between the BSA molecules, including hydrogen bonding (41%), charge-mediated (29%), salt bridging (26%) and hydrophobic bonding (4%) accounted for the high protein-protein interaction energy (Supplementary Figs. 7 and 8). The presence of additives such as urea<sup>42</sup> and sodium dodecyl sulfate (SDS)<sup>43</sup> disrupted 2D BSA/PVA microphase separation, while high concentrations of 1,6-hexanediol, which is known to disrupt hydrophobic interactions<sup>44</sup>, had minimal effect on lateral phase separation (Supplementary Fig. 9).

### Interfacial microphase domain structure and dynamics

Given that the discontinuous microdomains formed by lateral phase separation on the oil droplets were morphologically irregular rather than circular (minimal interface energy)<sup>45</sup>, we used fluorescence recovery after photo-bleaching (FRAP) to determine the fluidity of 5-([4,6-dichlorotriazin-2-yl]amino)fluorescein hydrochloride (DTAF)-labeled BSA and DTAF-PVA adsorbed independently at the surface of tributyrin droplets in water. The fluorescence intensity of PVA at the oil/water interface was almost completely recovered within 30 s (Fig. 2a, c), while no detectable fluorescence intensity recovery was observed for BSA even after 600 s (Fig. 2b, d); these observations were consistent with the presence of a fluid phase or non-mobile gel-like microstructure, respectively. The diffusion coefficient of the surface-adsorbed PVA molecules was  $0.94 \pm 0.19 \mu\text{m}^2/\text{s}$  (Fig. 2e and Supplementary Fig. 10), which was comparable to values determined for

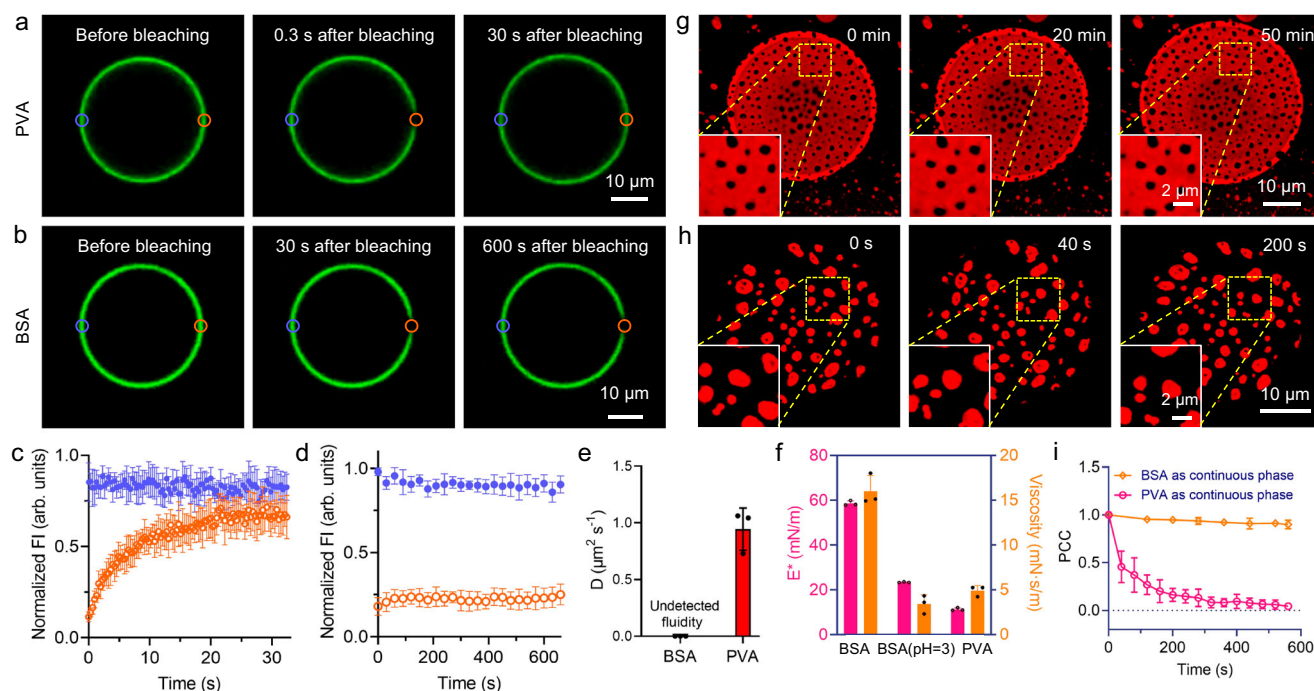


**Fig. 2 | Interfacial microphase domain structure and dynamics.** CLSM fluorescence images showing a single DTAF-labeled (green fluorescence) PVA-coated tributyrin microdroplet before bleaching (left) and 0.3 (middle) and 30 s (right) after laser-induced bleaching (a); corresponding CLSM images for a single DTAF-labeled BSA-coated tributyrin microdroplet before bleaching (left) and 30 (middle) and 600 s (right) after bleaching are shown in (b). The laser-induced bleaching is highly localized (orange circles); non-activated regions (control) are also shown (blue circle). c, d Corresponding FRAP profiles showing time-dependent changes in fluorescence intensity (FI) recorded from the orange and blue circles shown in (a) and (b), respectively. Fluid and gel-like states are observed for the PVA and BSA surface layers, respectively. e Diffusion coefficients of PVA and BSA at the tributyrin/water interface confirming the gel or fluid states of the microphase-separated BSA or PVA domains, respectively. f Plots of complex modulus ( $E^*$ ) and viscosity of BSA and PVA microphases at pH = 7 and 3 (BSA only) at the air/water interface. CLSM fluorescence images for oil droplets with BSA (g) or PVA (h) continuous

phases showing immobile or mobile microphase-separated PVA and BSA domains, respectively; Insets: Enlarged view of the yellow dashed area; RBITC-BSA, red fluorescence. i Changes of Pearson's correlation coefficient (PCC) over time showing the relationship of the microphase-separated state compared to the initial states. A PCC value close to 1.0 indicates that the fluorescence signals recorded at the same positions at different times and at time  $t = 0$  are highly overlapping, while fluorescence signals approaching zero indicate that the two fluorescence signals are not correlated. The PCC values maintain near to 1.0 over time, which demonstrate that the relative position of the PVA domains did not change. The PCC values gradually decrease to zero due to changes in the relative positions of the discontinuous BSA domains. Data in (c–f) and (i) are presented as mean values  $\pm$  SD, error bars indicate standard deviations ( $n = 3$  independent experiments). All relevant experiments are performed independently three times with similar results. Source data are provided as a Source Data file.

phospholipids at oil/water interfaces<sup>41</sup>. The complex modulus ( $E^*$ ) and viscosity ( $\mu$ ) of the BSA phase ( $E^* = 58.6$  mN/m,  $\mu = 16.0$  mN·s/m) were considerably larger than those determined for PVA ( $E^* = 11.3$  mN/m, and  $\mu = 4.9$  mN·s/m) (Fig. 2f), consistent with the increased intermolecular interactions associated with the protein domains. The time-dependent changes in the relative positions of discontinuous PVA or BSA microdomains on oil droplet surfaces at pH 7 were determined by 3D confocal microscopy imaging. The data indicated that the 2D PVA-in-BSA microstructures remained arrested in shape, size and position (Fig. 2g) and showed no fusion between the discontinuous PVA domains after being stored at room temperature in the dark for over two years. (Supplementary Fig. 11), consistent with the low mobility of the gel-like BSA continuous phase. In contrast, the relative positions of the discontinuous BSA domains present in floating BSA-in-PVA microstructures changed over a period of hundreds of seconds (Fig. 2h, i).

The 2D trajectories of the BSA rafts across the oil/water interface were statistically determined and shown to follow Brownian motion

with an almost linear relationship between the mean squared displacement (MSD) values and time, which were modulated by the size of the BSA domains (Fig. 3a and Supplementary Fig. 12). To ensure adequate statistical numbers, the BSA rafts on each microdroplet were divided into two groups according to their area with each group comprising 50% of the population; consequently, the group containing the smaller 50% of the domains exhibited a 1.2 times increase in MSD after 50 s of movement compared to the set comprising the larger 50% of islands. As each BSA raft was surrounded by many other protein domains, the movement was more typical of restricted Brownian motion<sup>21,46</sup>. The extent of deviation from regular Brownian motion was classified by an anomalous exponent ( $\alpha = 1$  (regular),  $\alpha < 1$  (restricted)). Plots of  $\alpha$  against area ratio (ie; surface area of BSA domain/total surface area of microdroplet) of the discontinuous BSA microdomains confirmed that the crowded array of BSA rafts restricted 2D Brownian motion of the protein rafts with larger area ratios associated with increased levels of restriction (lower  $\alpha$  values) (Fig. 3b and

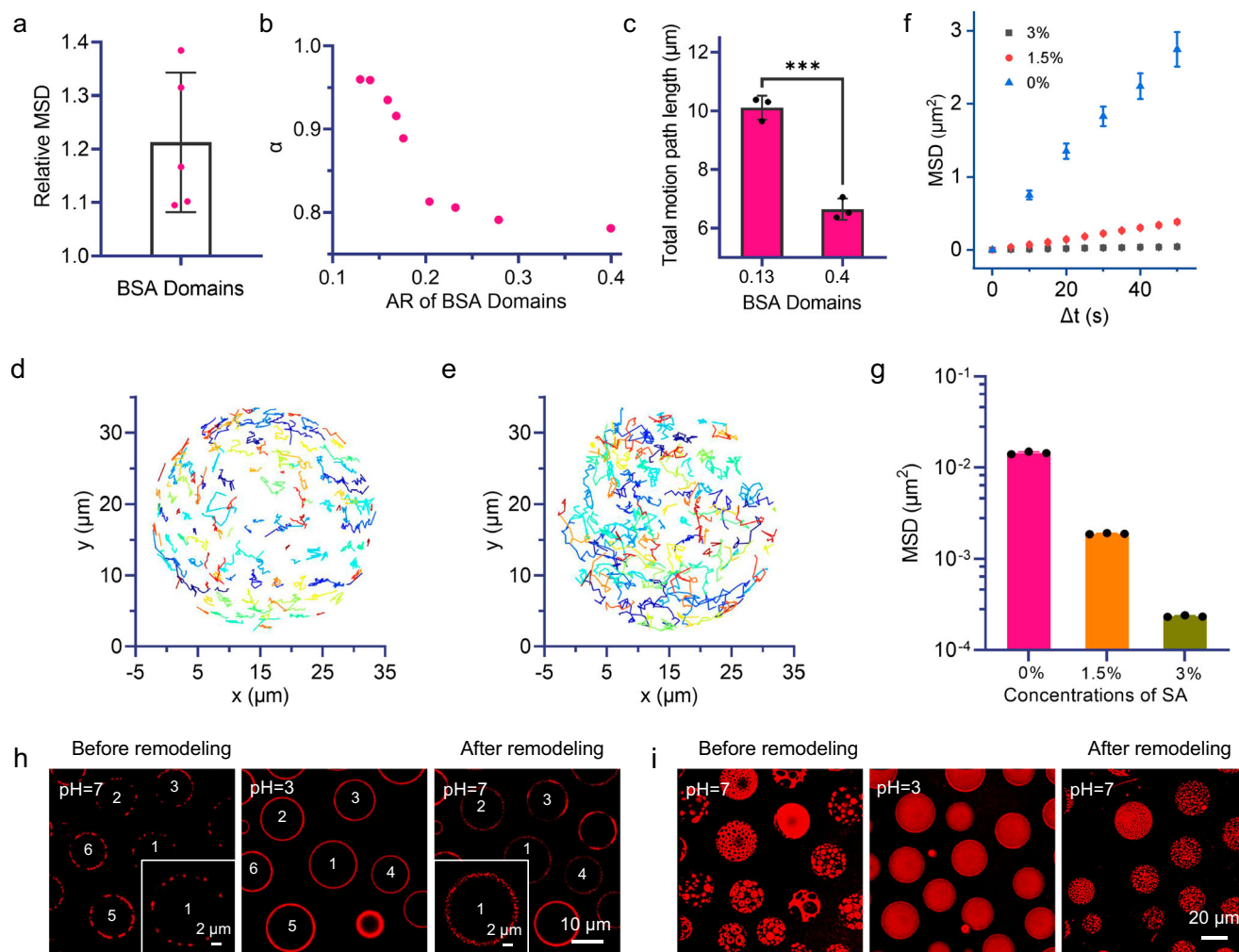


**Fig. 3 | Motility of microphase-separated BSA rafts on oil droplet surfaces.**

**a** Relative mean squared displacement (MSD) ratios of BSA domain size (smaller 50% of population): BSA domain size (larger 50%) determined for oil droplet-supported lateral BSA-in-PVA microstructures. **b** Anomalous exponent ( $\alpha$ ) of discontinuous BSA domains determined at different area ratios (AR). **c** Total motion path length of discontinuous BSA domains for AR values of 0.13 and 0.40. Trajectories of floating BSA rafts for AR values of 0.13 (**d**) or 0.40 (**e**). **f** MSD plot of Brownian motion of BSA domains at 0, 1.5, or 3% sodium alginate (SA) solutions. **g** Diffusion coefficient ( $D_r$ ) of BSA domains in 0, 1.5 or 3% SA solutions. **h** In-situ CLSM fluorescence images showing changes in the configuration of lateral BSA-in-PVA microstructures floating on tributyrin oil microdroplets (BSA, 4 mg/mL; PVA,

0.6 mg/mL) at an initial pH of 7 (left), followed by acidification to pH 3 (middle) and then a decrease back to pH 7 (right). Identical numbers in the images indicate the same droplet. **i** 3D fluorescence microscopy top view images of floating BSA-in-PVA microstructures recorded at an initial pH of 7 (left), and after acidification to pH 3 (middle) followed by increasing the pH back to 7 (right). Differences in (**c**) calculated by unpaired *T*-test (two-sided), \*\*\* $p < 0.001$ . Data in (**a**, **c**, **f**, **g**) are presented as mean values  $\pm$  SD, error bars indicate standard deviations ( $n = 5$  independent experiments in (**a**),  $n = 3$  independent experiments in **c**, **f**, **g**). All relevant experiments are performed independently at least three times with similar results. Source data are provided as a Source Data file.



Supplementary Fig. 12). For example, the average distance traveled during 50 s for an area ratio of 0.13 ( $\alpha = 0.96$ ) was 10  $\mu\text{m}$  compared with ca. 7  $\mu\text{m}$  at 0.40 ( $\alpha = 0.78$ ) (Fig. 3c). The former system also exhibited longer trajectories that overlapped between different domains, indicating dynamical changes in the relative spatial positions of the protein rafts (Fig. 3d, e). The average diffusion coefficient of BSA domains with an average size of 1.33  $\mu\text{m}$  for an area ratio of 0.13 was  $1.76 \times 10^{-2} \mu\text{m}^2/\text{s}$  (Supplementary Fig. 12). Interestingly, the 2D translational motion of the BSA rafts was decreased when the viscosity of the surrounding aqueous phase increased (Supplementary movie S2). For example, the MSD in aqueous solution ( $1.4 \times 10^{-2} \mu\text{m}^2/\text{s}$ ) was an order of magnitude larger than the diffusion coefficient calculated in 1.5 wt% sodium alginate solution ( $1.89 \times 10^{-3} \mu\text{m}^2/\text{s}$ ); increasing the alginate concentration to 3 wt% further restricted domain movement ( $2.3 \times 10^{-4} \mu\text{m}^2/\text{s}$ ) (Fig. 3f, g and Supplementary Fig. 13).

Translational movement of the BSA domains through the floating phase-separated microstructure resulted in inter-domain collisions and partial aggregation of the gel-like protein rafts into irregular clusters. The degree of aggregation was reversible and became more pronounced at pH values close to the isoelectric point of BSA (pH 4.7) (Supplementary Fig. 14), indicating that electrostatic repulsion between apposed edges of the BSA domains played an important role in minimizing aggregation of the motile protein domains under neutral pH conditions. Consequently, at high positive or negative zeta potential values, for example at pH values of 3.5 or 9.5, respectively, repulsion between the protein domains was sufficiently high that the floating BSA-in-PVA microstructures transformed into a homogeneous BSA/PVA shell around the oil droplets (Fig. 3h and Supplementary Fig. 15). This was consistent with decreases in  $\zeta^*$  and  $\mu$  to values of 23.2 and 3.8 mN·s/m, respectively, at pH 3 (see Fig. 2f). Interestingly, in situ transformation of the homogeneous BSA/PVA shell by returning the pH to 7 produced a 2D BSA-in-PVA phase-separated microstructure with increased morphological regularity (Fig. 3h and Supplementary movie S3). Specifically, the mean size and size distribution of the BSA domains decreased and narrowed, respectively, after remodeling (Fig. 3i). The phase separation was not affected by different buffers or changes in salt concentration, which ruled out the effect of these additives on the pH-mediated changes in phase separation (Supplementary Figs. 16, 17). In addition, nested microstructures such as PVA-in-BSA-in-PVA were almost absent after remodeling, being replaced by the binary PVA-in-BSA and BSA-in-PVA floating microphases (Supplementary Fig. 18), indicating that the nested microphase-separated modes were kinetically arrested.

### Floating microphase-separated interfacial reaction platforms

Having established reconfigurable oil droplet-supported platforms of 2D BSA/PVA phase-separated microstructures, we sought to develop floating continuous protein/PVA heterostructures capable of spatially modulated interfacial enzyme catalysis. In the presence of PVA, proteins such as alkaline phosphatase,  $\beta$ -galactosidase, human serum albumin, catalase, lysozyme, myoglobin and GFP spontaneously underwent lateral microphase separation on the surface of tributyrin oil droplets at pH 7 (Supplementary Fig. 19). In contrast, spatially homogeneous mixtures of PVA and glucose oxidase (GOx), PVA and horseradish peroxidase (HRP) or PVA and calmodulin (CaM) were observed at the oil droplet/water interface (Supplementary Fig. 19). The absence of 2D microphase separation was attributed to weak protein-protein intermolecular attractions or strong protein/PVA interactions, or both. Nonetheless, these proteins were enriched in the BSA domains (Supplementary Fig. 19).

Given these observations, we generated oil droplet-supported 2D reaction platforms with spatially distributed enzymes by specifically enriching the discontinuous BSA domains of floating BSA-in-PVA microstructures with GOx and HRP catalytic sites (Fig. 4a–c) and

investigated the influence of interfacial liquid-liquid phase separation and microstructural remodeling on enzyme cascade activity on the surface of oil microdroplets comprising three different surface configurations: (i) an immobile homogeneous GOx/HRP/BSA platform; (ii) an as-prepared GOx/HRP-enriched BSA-in-PVA microphase-separated platform with restricted domain motility; or (iii) a remodeled GOx/HRP-enriched BSA-in-PVA microphase-separated platform with increased domain dynamics (Fig. 4d). The level of enzyme loading was the same for the homogeneous and microphase-separated oil droplet platforms (Supplementary Fig. 20). The mole percentages of GOx, HRP and BSA were 12, 10, and 78%, respectively, in the microphase-separated platforms.

Measurements of the mean squared displacements and diffusion coefficients before and after pH-mediated remodeling indicated that the GOx/HRP-enriched BSA-based domains became more motile after annealing, which was attributed to the decrease in mean size and more uniform size distribution of the protein domains (Fig. 4e, f). To initiate the enzyme cascade reaction, glucose was added to suspensions of the different coated oil droplets in the presence of Amplex red at pH 7 and 25 °C. As the enzyme cascade proceeds by diffusive transfer of GOx-mediated  $\text{H}_2\text{O}_2$  to HRP and subsequent peroxidation of Amplex red, we determined the influence of changes in the oil droplet-supported microphase domain structure and dynamics by using CLSM to monitor the initial rates of production of resorufin (Fig. 4g and Supplementary Fig. 21). Specifically, under constant enzyme concentrations, the initial reaction rates were 1.5 times slower on the homogeneous GOx/HRP shell compared with the as-prepared floating GOx/HRP/BSA microphase-separated catalytic platform. Moreover, the increased level of domain movement in the remodeled phase-separated platform increased the initial reaction rate 1.3-fold compared with the non-annealed counterpart. The results suggest that decreasing the distance between the enzymes by enrichment in the BSA gel-like domains of the floating phase-separated microstructure facilitates diffusion of  $\text{H}_2\text{O}_2$  from GOx to HRP, thereby increasing the initial rates compared with oil droplets coated in a homogeneous reaction platform. The possibility of translational movements in the 2D phase-separated platforms could also decrease the  $\text{H}_2\text{O}_2$  diffusion time, thereby increasing local mass transport<sup>47</sup>. Consequently, the enhanced Brownian motion of the protein domains in the annealed GOx/HRP/BSA-in-PVA microphase further promotes transfer of  $\text{H}_2\text{O}_2$  from GOx to HRP to promote the initial reaction kinetics. In contrast to previous reports<sup>48–50</sup>, although our platform does not achieve large-scale regulation of enzyme reaction rates, the phase separation-mediated changes in activity of the microdroplets provides a platform and strategy for regulating the surface structure and function of oil/water droplets.

### Discussion

We describe a general approach to the use of oil-droplet templating to generate a range of floating protein-polymer 2D continuous microstructures by liquid-liquid lateral phase separation. The procedure produces a range of different phase-separated modes with variable interfacial domain structures and dynamics, and can be extended to different types of oil such as dodecane, tetradecane, trichlorobenzene, trichloromethane, n-hexane, kerosene (Supplementary Fig. 22) as well as non-ionic surfactant polymers such as poly(poly(ethylene glycol) methyl ether methacrylate)-*b*-poly(N-isopropylacrylamide) (PPEGMA-*b*-PNIPAAm)<sup>5</sup> and Tween 80 (Supplementary Fig. 23). The decreased fluidity of the BSA gel-like domains facilitates the formation of tessellated heterostructures consisting of a continuous protein 2D mesh, or an array of discrete protein rafts that exhibit translational motion across the oil droplet surface depending on their size, area ratio and viscosity of the aqueous medium. Electrostatic interactions between the apposed edges of the BSA rafts determine the level of reversible aggregation displayed in the microphase structures. Moreover, enzymes can be immobilized

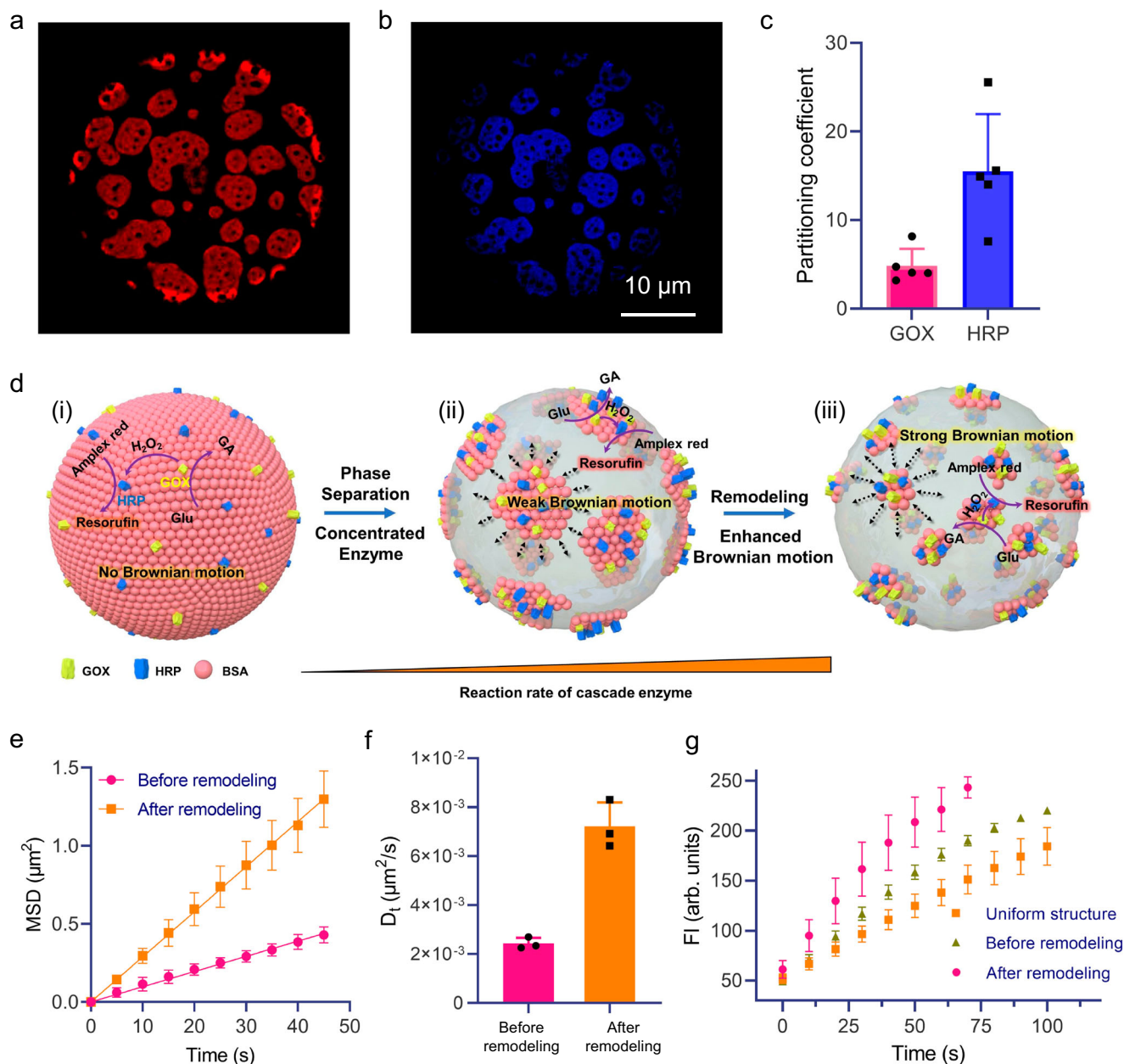


**Fig. 4 | Floating microphase-separated interfacial reaction platforms.** 3D top view of CLSM fluorescence images of a single tributyrin oil droplet showing partitioning and colocation of RBITC-labeled GOx (red fluorescence) (**a**) and ATTO 425-labeled HRP (blue fluorescence) (**b**) in the discontinuous BSA domains of a floating phase-separated microstructure. **c** Partition coefficients of RBITC-GOx ( $\approx 4.8$ ) and ATTO 425-HRP ( $\approx 15.5$ ) determined from the concentration ratios,  $[\text{protein}]_{\text{BSA}}/[\text{protein}]_{\text{PVA}}$ . **d** Illustration showing influence of protein domain formation and lateral motility of floating oil droplet-supported reaction platforms on surface-localized enzyme cascade reactions; immobile homogeneous GOx/HRP/BSA platform; (left), as-prepared GOx/HRP-enriched BSA-in-PVA microphase-separated platform with restricted domain motility (middle) and a remodeled GOx/HRP-

enriched BSA-in-PVA microphase-separated platform with increased domain dynamics (right). **e** MSD plots of discontinuous GOx/HRP/BSA domains before and after remodeling of a protein-in-PVA microphase-separated reaction platform. **f** Diffusion coefficient ( $D_t$ ) of protein microphases before and after remodeling. **g** Plot of time-dependent changes in fluorescence intensity (FI) associated with resorufin production on homogeneous or microphase-separated GOx/HRP/BSA-in-PVA floating platforms before and after remodeling. Data in (c and e–g) are presented as mean values  $\pm$  SD, error bars indicate standard deviations ( $n = 5$  independent experiments in (c),  $n = 3$  independent experiments in e–g). All relevant experiments are performed independently at least three times with similar results. Source data are provided as a Source Data file.

in the discontinuous BSA domains to produce floating microphase-separated 2D reaction scaffolds that can be tuned for interfacial catalysis. Taken together, our work on droplet-templated liquid-liquid lateral microphase separation provides a platform for spontaneously generating discrete spatially patterned 2D protein/polymer heterostructures and advances the microengineering of oil droplet/water interfaces for use in biocatalytic processing.

## Methods

### Characterization methods

Confocal fluorescence images were recorded on a Leica SP8 Laser scanning confocal microscope (Germany). Optical tensiometers (OSA 100, China) were employed to test the interfacial tensions and the interfacial rheological properties of emulsion droplets stabilized by BSA and PVA. Image J (FIJI) software (Version 1.44p, USA) was

employed to measure the velocities and trajectories of BSA islands. Micromanipulation was carried out on fluorescence microscope (OLYMPUS, IX73, Japan) equipped with a micromanipulation system (Eppendorf, TransferMan 4r, Germany).

### Preparation of oil-in-water microdroplets

BSA (labeled with dyes) and PVA at a range of concentrations were co-dissolved in water at pH = 7.0 (10 mM PBS). 200  $\mu$ L of the aqueous mixture was then added to 20  $\mu$ L of an oil phase (tributyrin in most cases) in an EP tube followed by vigorous shaking. After settling naturally for 5 min, microdroplets deposited at the bottom of the tube were placed into PBS (10 mM, pH = 7) to remove extraneous proteins and polymers that were not adsorbed to the oil-water interface.

### Determination of interfacial tension and interfacial rheology

An optical surface analyzer was used to determine the complex modulus ( $E^*$ ) and viscosity of BSA or PVA at the air/water interface by the pendant drop method. The complex modulus ( $E^*$ ) and viscosity were determined by periodically changing the volume of the pendant drop. Specifically, an aqueous pendant drop (80  $\mu$ L) containing BSA (4 mg/mL, pH = 7 or 3) or PVA (0.6 mg/mL, pH = 7) was produced in humid air and the volume kept constant during 2-h equilibration. A sinusoidal oscillation of the volume of droplet was performed by the pump. The amplitude was 4  $\mu$ L and the frequency was 0.1 Hz. The interfacial complex modulus ( $E^*$ ) and viscosity was calculated automatically by the instrument.

The interfacial tension of BSA and PVA at the interface of tributyrin/water was also recorded by the optical surface analyzer. Tributyrin pendant drop (20  $\mu$ L) was produced in the solution of BSA (4 mg/mL, pH = 7) and PVA (0.6 mg/mL, pH = 7). The interfacial tensions were measured after 2 h of incubation.

### Molecular dynamics (MD) simulations

The force field was constructed by ORCA, MultiWFN and Gromacs. The force field of BSA was AMBER99SB-ILDN constructed by Gromacs. PVA and tributyrin were structurally optimized using ORCA. The function was B3LYP and the base group def2-TZVP. RESP charges were assigned using MultiWFN and the GAFF force field of the molecule was generated. The simulation was performed using Gromacs 2021.7. The size of the simulation box was 22 nm  $\times$  22 nm  $\times$  27 nm, which contained 4 BSA, 26 PVA and 7709 tributyrin and 136,794 H<sub>2</sub>O. The water model was SPC. 64 Na<sup>+</sup> were used to balance the system charge to make the system process electrically neutral.

During the simulation, 50,000 steps of energy minimization were first performed to eliminate bad contacts in the initial structures. Then, two equilibrium simulations were carried out: NVT (constant volume) and NPT (constant pressure). Finally, MD simulations were performed for 200 ns at 298.15 K and 1 bar pressure. The finished simulation integrated Newton's equations of motion using a leapfrog algorithm with an integration time step of 2 fs. The finished product was simulated using the V-rescale temperature coupling method and the Parrinello-Rahman pressure coupling method. The nearest neighbor search was performed using the Verlet method. The cutoff radius for Coulomb and van der Waals interactions was 1.4 nm. Long-range electrostatic interactions were calculated using the PME method. Long-range dispersion correction was used for energy and pressure. After the simulation, the simulation trajectories were visualized using the VMD 1.9.4 program.

### Fluorescence labeling of proteins

A selected protein (10 mg) was dissolved in 5 mL of PBS (50 mM, pH = 8) and then 50  $\mu$ L of a fluorescent dye (dissolved in DMSO, 1 mg/mL, RBITC, Atto 425 or DTAF) was added dropwise. The mixture was stirred at room temperature for 5 h and purified by dialysis with deionized

water for 36 h to remove unreacted fluorescent dye. Any precipitates were removed by a syringe filter (Nylon, 0.2  $\mu$ m) and the protein powder was obtained by freeze drying.

### Fluorescence recovery after photobleaching (FRAP)

BSA-DTAF-stabilized tributyrin microdroplets were prepared. The fluorescence was irreversibly bleached with 100% fluorescent intensity by CLSM. The fluorescence recovery images were taken at an interval of 30 s. Confocal software (Leica) was used to calculate the fluorescence intensity changes with time.

Because PVA-DTAF did not undergo phase separation with BSA, we prepared PVA-stabilized microdroplets with unlabeled PVA. Specifically, 200  $\mu$ L of PVA (1 mg/mL) was mixed with 20  $\mu$ L of tributyrin followed by vigorous shaking. After 10 min sedimentation, 200  $\mu$ L of PBS (50 mM, pH = 8) was added to adjust the pH of the solution followed by addition of 1  $\mu$ L of DTAF (dissolved in DMSO, 1 mg/mL). In this way, the impact of fluorescence labeling on the liquidity of PVA could be reduced. The redundant dye and PVA were removed by changing the supernatant to water. The photobleaching procedure was also used with BSA-DTAF-stabilized tributyrin microdroplets except the fluorescence recovery images were recorded every 0.3 s as the fluorescence recovery process was very fast.

Diffusion coefficients were calculated according to a previous method<sup>51</sup>. Specifically, the fluorescence intensity of the membrane near the bleaching point was measured by image J. The curve was fitted to a Gaussian function. The peak height of the curve ( $C_0$ ) represented the concentration of the bleached dyes, and  $R_0$  represented the parametric half-width of the Gaussian equation when  $t = 0$  s ( $R_0 = 0.8493218 \times \text{FWHM}$  (full width at half maximum)).  $(C_{(t=0)}/C_{(t)})^2$  and  $t$  were fitted linearly according to formula 1-1. The slope was  $8D/R_0^2$ . The diffusion coefficient ( $D$ ) was calculated according to the slope.

$$\left(\frac{C_{(t=0)}}{C_{(t)}}\right)^2 = 1 + \frac{8D}{R_0^2}t \quad (1)$$

### Remodeling of two-dimensional phase separation

200  $\mu$ L of an aqueous solution containing BSA (4 mg/mL) and PVA (0.6 mg/mL) was mixed with 20  $\mu$ L of tributyrin. After shaking and settling, 5  $\mu$ L of microdroplets and 10  $\mu$ L of citrate buffer solution (0.1 M, pH = 3) were uniformly mixed and incubated for 3 min to transform the phase-separated microstructure into a homogeneous structure. Then, 50  $\mu$ L of PBS (0.05 M, pH = 8) was added to change the pH of the mixture to around 7 and the mixture incubated for 5 min to promote the re-formation of the phase-separated state.

### Two-dimensional phase separation in different buffers and salt concentrations

Oil-in-water microdroplets were prepared as described above (section, Preparation of oil-in-water microdroplets). 5  $\mu$ L of microdroplets were added to 500  $\mu$ L of different aqueous solutions (PBS, 50 mM, pH = 3 or 7; citrate buffer, 100 mM, pH = 3 or 7; distilled water; NaCl, 60, 300 or 3000 mM) and the phase-separated structures observed by CLSM.

### Brownian motion statistics of protein domains

The Brownian motion of the BSA domains was recorded by a series of CLSM 3D images with the same time interval. To obtain a more accurate Brownian motion trajectory, the time interval between the two 3D images was as small as possible. While maintaining clarity, a number of steps were taken to enhance the speed of scanning, including setting the scan format of the CLSM to 128 $\times$ 128, opening bidirectional x, only capturing the lower part of the microsphere and setting the steps of



the 3D scan to twenty-eight. Finally, the time interval of the 3D images was set to 5 s. To facilitate the statistics of the Brownian motion trajectories, we recorded overhead views of the Brownian motion process by CLSM and calculated the trajectories. To reduce the statistical error, we captured CLSM images of the lower part of the sphere with the radius angle around 90° (the red solid line in Supplementary Fig. 24), so that the Brownian motion on the sphere surface can be approximated to the Brownian motion on the plane.

### Trajectory analysis of Brownian motion

A series of CLSM 3D images were made into movies with movie maker. The trajectories, speed and motion distance were calculated by FIJ. Briefly, the movie was imported into FIJ. After determining the scale, the area of interest in the movie was copied and converted to 8-bits. Adjustment of the threshold parameters was used to find settings that would detect all protein domains and a limited number of spurious detections. The plugin trackmate was utilized to calculate information such as trajectories, speed of protein domains. The trajectories were exported to XML file for further analysis. Finally, the exported xml file was inputted to matlab and the MSD information calculated.

### Area ratio statistics of BSA domains

Area ratio statistics of the BSA domains was performed by FIJ. Images after threshold setting were obtained as described above for the Trajectory analysis of Brownian motion. For the phase separation types PVA-in-BSA-in PVA and hybrid structures, the internal PVA phase was also counted as a part of protein phase for the determination of the area statistics. This was because the PVA phase caused crowding of the BSA domains which limited Brownian motion. The Fill Holes setting was performed to fill the PVA holes inside the BSA phase. The total area of BSA phase was calculated using Analyze Particles function in FIJ. The area ratio of BSA domains was obtained by dividing the total area of the BSA domain by the total area of the microdroplet.

### The partition coefficient of RBITC-GOx and ATTO 425-HRP

The partition coefficient was determined as  $[\text{protein}]_{\text{BSA}}/[\text{protein}]_{\text{PVA}}$ , where  $[\text{protein}]_{\text{BSA}}$  and  $[\text{protein}]_{\text{PVA}}$  were the concentrations of RBITC-GOx and ATTO 425-HRP in the BSA and PVA phases, respectively. The fluorescence intensity was proportional to the protein concentration of the substance. Hence, the partition coefficient was approximately determined as fluorescence intensity in BSA phase/fluorescence intensity in PVA phase.

### Construction of enzyme reaction platforms based on lateral phase separation

The GOx/HRP cascade reaction rates were determined using three droplet-based platforms: (a) an immobile homogeneous GOx/HRP/BSA platform (homogeneously coated emulsion droplets), (b) an as-prepared GOx/HRP-enriched BSA-in-PVA microphase-separated platform (no remodeling; restricted domain motility), and (c) a remodeled GOx/HRP-enriched BSA-in-PVA microphase-separated platform with increased domain dynamics. Fluorescence intensity measurements on the droplet membranes were used to ensure that the homogeneously coated emulsion droplets and floating phase-separated microstructures contained the same number of enzymes (Supplementary Fig. 20)). The preparation procedure was as described above (see section, Preparation of oil-in-water microdroplets). Solutions of RBITC-labeled enzymes (HRP 2.3 mg/mL, GOx 10.8 mg/mL) and unlabeled BSA (10 mg/mL) were mixed at a volume ratio of 1 to 19 as the aqueous phase of a homogeneous oil-in-water emulsion. For the preparation of floating phase-separated microstructure emulsion droplets, 60  $\mu\text{L}$  of a mixture of RBITC-labeled enzymes (HRP 2.3 mg/mL, GOx

10.8 mg/mL) and unlabeled BSA (10 mg/mL) with different volume ratios was mixed with 140  $\mu\text{L}$  PVA (1 mg/mL) and used as the aqueous phase of an oil-in-water emulsion. When the volume ratio of the enzyme solution and unlabeled BSA was 1:3, the mean fluorescence intensity of the membrane (ca. 95.2) was equal to that of the homogeneous emulsion, indicating similar levels of enzyme loading (Supplementary Fig. 20d). Remodeling of the floating phase-separated microstructures was undertaken as described above (section, Remodeling of two-dimensional phase separation). For all three platforms, 10  $\mu\text{L}$  of oil droplets were mixed with 1  $\mu\text{L}$  of Amplex red (200  $\mu\text{M}$ ) and 1  $\mu\text{L}$  of glucose (500  $\mu\text{M}$ ). CLSM was used to determine the fluorescence intensity changes associated with the product resorufin.

### Reporting summary

Further information on research design is available in the Nature Portfolio Reporting Summary linked to this article.

### Data availability

The experimental data generated in this study are available as the Supplementary Information. Source data are provided with this paper.

### References

- Venkataramani, D., Tsulaia, A. & Amin, S. Fundamentals and applications of particle stabilized emulsions in cosmetic formulations. *Adv. Colloid Interface Sci.* **283**, 102234 (2020).
- Tan, C. & McClements, D. J. Application of advanced emulsion technology in the food industry: a review and critical evaluation. *Foods* **10**, 812 (2021).
- Zhou, Y., Yin, D., Chen, W., Liu, B. & Zhang, X. A comprehensive review of emulsion and its field application for enhanced oil recovery. *Energy Sci. Eng.* **7**, 1046–1058 (2019).
- Yang, Z., Wei, J., Sobolev, Y. I. & Grzybowski, B. A. Systems of mechanized and reactive droplets powered by multi-responsive surfactants. *Nature* **553**, 313–318 (2018).
- Chen, H. et al. Construction of hybrid Bi-microcompartments with exocytosis-inspired behavior toward fast temperature-modulated transportation of living organisms. *Angew. Chem., Int. Ed.* **60**, 20795–20802 (2021).
- Zarzar, L. D. et al. Dynamically reconfigurable complex emulsions via tunable interfacial tensions. *Nature* **518**, 520–524 (2015).
- Wang, X., Liu, X. & Huang, X. Bioinspired protein-based assembling: toward advanced life-like behaviors. *Adv. Mater.* **32**, 2001436 (2020).
- Huang, X. et al. Interfacial assembly of protein-polymer nano-conjugates into stimulus-responsive biomimetic protocells. *Nat. Commun.* **4**, 2239 (2013).
- Rodríguez-Arco, L., Li, M. & Mann, S. Phagocytosis-inspired behaviour in synthetic protocell communities of compartmentalized colloidal objects. *Nat. Mater.* **16**, 857–863 (2017).
- Wang, X. et al. Synthetic-cell-based multi-compartmentalized hierarchical systems. *Small Methods* **7**, 2201712 (2023).
- Choi, S., Meyer, M. O., Bevilacqua, P. C. & Keating, C. D. Phase-specific RNA accumulation and duplex thermodynamics in multi-phase coacervate models for membraneless organelles. *Nat. Chem.* **14**, 1110–1117 (2022).
- Keating, C. D., Martin, N. & Santore, M. M. Editorial overview: coacervates and membraneless organelles. *Curr. Opin. Colloid Interface Sci.* **56**, 101527 (2021).
- Hindley, J. W. et al. Building a synthetic mechanosensitive signaling pathway in compartmentalized artificial cells. *Proc. Natl. Acad. Sci.* **116**, 16711–16716 (2019).
- Chao, Y. & Shum, H. C. Emerging aqueous two-phase systems: from fundamentals of interfaces to biomedical applications. *Chem. Soc. Rev.* **49**, 114–142 (2020).



15. Yewdall, N. A., André, A. A. M., Lu, T. & Spruijt, E. Coacervates as models of membraneless organelles. *Curr. Opin. Colloid Interface Sci.* **52**, 101416 (2021).
16. Mashayekhi, F., Meyer, A. S., Shiigi, S. A., Nguyen, V. & Kamei, D. T. Concentration of mammalian genomic DNA using two-phase aqueous micellar systems. *Biotechnol. Bioeng.* **102**, 1613–1623 (2009).
17. Albertsson, P. E. R. A. Partition of proteins in liquid polymer–polymer two-phase systems. *Nature* **182**, 709–711 (1958).
18. Li, J. et al. Programmable spatial organization of liquid-phase condensations. *Chem* **8**, 784–800 (2022).
19. Xu, Z. et al. Photosynthetic hydrogen production by droplet-based microbial micro-reactors under aerobic conditions. *Nat. Commun.* **11**, 5985 (2020).
20. Zhao, C. et al. Membranization of coacervates into artificial phagocytes with predation toward bacteria. *ACS Nano* **15**, 10048–10057 (2021).
21. Song, S., Llopis-Lorente, A., Mason, A. F., Abdelmohsen, L. & van Hest, J. C. M. Confined motion: motility of active microparticles in cell-sized lipid vesicles. *J. Am. Chem. Soc.* **144**, 13831–13838 (2022).
22. Zhang, S. et al. Engineering motile aqueous phase-separated droplets via liposome stabilisation. *Nat. Commun.* **12**, 1673 (2021).
23. Liu, Y. et al. Entropy-driven pattern formation of hybrid vesicular assemblies made from molecular and nanoparticle amphiphiles. *J. Am. Chem. Soc.* **136**, 2602–2610 (2014).
24. Lyu, X. et al. A gel-like condensation of Cidec generates lipid-permeable plates for lipid droplet fusion. *Dev. Cell* **56**, 2592–2606 (2021).
25. Chen, H. et al. Fusion-induced structural and functional evolution in binary emulsion communities. *Angew. Chem., Int. Ed.* **59**, 16953–16960 (2020).
26. Levental, I., Levental, K. R. & Heberle, F. A. Lipid rafts: controversies resolved, mysteries remain. *Trends Cell Biol.* **30**, 341–353 (2020).
27. Simons, K. & Toomre, D. Lipid rafts and signal transduction. *Nat. Rev. Mol. Cell Biol.* **1**, 31–39 (2000).
28. Mulcahy, L. A., Pink, R. C. & Carter, D. R. F. Routes and mechanisms of extracellular vesicle uptake. *J. Extracell. Vesicles* **3**, 24641 (2014).
29. Teruo, H. & Tsung-Ping, S.  $\sigma$ -1 Receptors ( $\sigma$ 1 binding sites) form raft-like microdomains and target lipid droplets on the endoplasmic reticulum: roles in endoplasmic reticulum lipid compartmentalization and export. *J. Pharmacol. Exp. Ther.* **306**, 718 (2003).
30. Garofalo, T. et al. Evidence for the involvement of lipid rafts localized at the ER-mitochondria-associated membranes in autophagosome formation. *Autophagy* **12**, 917–935 (2016).
31. Hedskog, L. et al. Modulation of the endoplasmic reticulum–mitochondria interface in Alzheimer’s disease and related models. *Proc. Natl. Acad. Sci.* **110**, 7916–7921 (2013).
32. Filipczak, N., Pan, J., Yalamarty, S. S. K. & Torchilin, V. P. Recent advancements in liposome technology. *Adv. Drug Deliv. Rev.* **156**, 4–22 (2020).
33. Zhu, Y., Cao, S., Huo, M., van Hest, J. C. M. & Che, H. Recent advances in permeable polymersomes: fabrication, responsiveness, and applications. *Chem. Sci.* **14**, 7411–7437 (2023).
34. He, Q., Vijayamohanan, H., Li, J. & Swager, T. M. Multifunctional photonic Janus particles. *J. Am. Chem. Soc.* **144**, 5661–5667 (2022).
35. Crowe, C. D. & Keating, C. D. Microfluidic control of coexisting chemical microenvironments within multiphase water-in-fluorocarbon droplets. *Langmuir* **38**, 1811–1820 (2022).
36. Huang, Y. & Huang, X. Biomolecule-based coacervates with modulated physiological functions. *Langmuir* **39**, 8941–8951 (2023).
37. Li, J., Liu, X., Abdelmohsen, L. K. E. A., Williams, D. S. & Huang, X. Spatial organization in proteinaceous membrane-stabilized coacervate protocells. *Small* **15**, 1902893 (2019).
38. Mason, A. F., Buddingh’, B. C., Williams, D. S. & van Hest, J. C. M. Hierarchical self-assembly of a copolymer-stabilized coacervate protocell. *J. Am. Chem. Soc.* **139**, 17309–17312 (2017).
39. Christian, D. A. et al. Spotted vesicles, striped micelles and Janus assemblies induced by ligand binding. *Nat. Mater.* **8**, 843–849 (2009).
40. Rideau, E., Wurm, F. R. & Landfester, K. Membrane engineering: phase separation in polymeric giant vesicles. *Small* **16**, 1905230 (2020).
41. Pontani, L.-L., Haase, M. F., Raczowska, I. & Bruijic, J. Immiscible lipids control the morphology of patchy emulsions. *Soft Matter* **9**, 7150–7157 (2013).
42. Wang, K. & Arntfield, S. D. Probing the molecular forces involved in binding of selected volatile flavour compounds to salt-extracted pea proteins. *Food Chem* **211**, 235–242 (2016).
43. Yan, J.-N. et al. Intermolecular interaction in the hybrid gel of scallop (*Patinopecten yessoensis*) male gonad hydrolysates and  $\kappa$ -carrageenan. *J. Food Sci.* **86**, 792–802 (2021).
44. Gao, Y., Li, X., Li, P. & Lin, Y. A brief guideline for studies of phase-separated biomolecular condensates. *Nat. Chem. Biol.* **18**, 1307–1318 (2022).
45. Veatch, S. L. & Keller, S. L. Separation of liquid phases in giant vesicles of ternary mixtures of phospholipids and cholesterol. *Bio-phys. J.* **85**, 3074–3083 (2003).
46. Metzler, R., Jeon, J.-H., Cherstvy, A. G. & Barkai, E. Anomalous diffusion models and their properties: non-stationarity, non-ergodicity, and ageing at the centenary of single particle tracking. *Phys. Chem. Chem. Phys.* **16**, 24128–24164 (2014).
47. Karshalev, E., Esteban-Fernández de Ávila, B. & Wang, J. Micro-motors for “chemistry-on-the-fly”. *J. Am. Chem. Soc.* **140**, 3810–3820 (2018).
48. Fu, J., Liu, M., Liu, Y., Woodbury, N. W. & Yan, H. Interenzyme substrate diffusion for an enzyme cascade organized on spatially addressable DNA nanostructures. *J. Am. Chem. Soc.* **134**, 5516–5519 (2012).
49. Zhao, Z. et al. Nanocaged enzymes with enhanced catalytic activity and increased stability against protease digestion. *Nat. Commun.* **7**, 10619 (2016).
50. Li, Y., Liu, L. & Zhao, H. Enzyme-catalyzed cascade reactions on multienzyme proteinosomes. *J. Colloid Interface Sci.* **608**, 2593–2601 (2022).
51. Negishi, M., Seto, H., Hase, M. & Yoshikawa, K. How does the mobility of phospholipid molecules at a water/oil interface reflect the viscosity of the surrounding oil? *Langmuir* **24**, 8431–8434 (2008).

## Acknowledgements

We thank the National Natural Science Foundation of China (Grant No. 22307030, 22171058, 52473109) the Fundamental Research Funds for the Central Universities (HIT.OCEF.2023040) and China-Germany Mobility Program (M-0470) and the China Postdoctoral Science Foundation (Grant nos. 2021M700998, 2023M730844) and the Heilongjiang Postdoctoral Foundation (No. LBH-Z21055) for financial support.

## Author contributions

H.C., W.W., and X.H. conceived the experiments; H.C., Z.H. performed the experiments; H.C., Z.H., S.W., M.Z., L.W., Y.L., X.W., Y.Z., M.L., X.L., S.M., and X.H. undertook data analysis; H.C., X.H., and S.M. wrote the manuscript.

## Competing interests

The authors declare no competing interests.

## Additional information

**Supplementary information** The online version contains supplementary material available at <https://doi.org/10.1038/s41467-025-57141-w>.

**Correspondence** and requests for materials should be addressed to Stephen Mann or Xin Huang.

**Peer review information** *Nature Communications* thanks Silvia Moreno and the other, anonymous, reviewers for their contribution to the peer review of this work. A peer review file is available.

**Reprints and permissions information** is available at <http://www.nature.com/reprints>

**Publisher's note** Springer Nature remains neutral with regard to jurisdictional claims in published maps and institutional affiliations.

**Open Access** This article is licensed under a Creative Commons Attribution-NonCommercial-NoDerivatives 4.0 International License, which permits any non-commercial use, sharing, distribution and reproduction in any medium or format, as long as you give appropriate credit to the original author(s) and the source, provide a link to the Creative Commons licence, and indicate if you modified the licensed material. You do not have permission under this licence to share adapted material derived from this article or parts of it. The images or other third party material in this article are included in the article's Creative Commons licence, unless indicated otherwise in a credit line to the material. If material is not included in the article's Creative Commons licence and your intended use is not permitted by statutory regulation or exceeds the permitted use, you will need to obtain permission directly from the copyright holder. To view a copy of this licence, visit <http://creativecommons.org/licenses/by-nc-nd/4.0/>.

© The Author(s) 2025